Spin Manipulation of Heterogeneous Molecular Electrocatalysts by an Integrated Magnetic Field for Efficient Oxygen Redox Reactions

Yu, Zixun; Zhang, Di; Wang, Yangyang; Liu, Fangzhou; She, Fangxin; Chen, Jiaxiang; Zhang, Yuefeng; Wang, Ruijie; Zeng, Zhiyuan; Song, Li; Chen, Yuan; Li, Hao; Wei, Li

Published in:
Advanced Materials

Published: 07/11/2024

Document Version:
Final Published version, also known as Publisher's PDF, Publisher's Final version or Version of Record

Published version (DOI):
10.1002/adma.202408461

Publication details:
Yu, Z., Zhang, D., Wang, Y., Liu, F., She, F., Chen, J., Zhang, Y., Wang, R., Zeng, Z., Song, L., Chen, Y., Li, H., & Wei, L. (2024). Spin Manipulation of Heterogeneous Molecular Electrocatalysts by an Integrated Magnetic Field for Efficient Oxygen Redox Reactions. *Advanced Materials*, *36*(45), Article 2408461. https://doi.org/10.1002/adma.202408461

ADVANCED MATERIALS
www.advmat.de

Spin Manipulation of Heterogeneous Molecular Electrocatalysts by an Integrated Magnetic Field for Efficient Oxygen Redox Reactions

Zixun Yu, Di Zhang, Yangyang Wang, Fangzhou Liu, Fangxin She, Jiaxiang Chen, Yuefeng Zhang, Ruijie Wang, Zhiyuan Zeng, Li Song, Yuan Chen, Hao Li,* and Li Wei**

Understanding the spin-dependent activity of nitrogen-coordinated single metal atom (M-N-C) electrocatalysts for oxygen reduction and evolution reactions (ORR and OER) remains challenging due to the lack of structure-defined catalysts and effective spin manipulation tools. Herein, both challenges using a magnetic field integrated heterogeneous molecular electrocatalyst prepared by anchoring cobalt phthalocyanine (CoPc) deposited carbon black on polymer-protected magnet nanoparticles, are addressed. The built-in magnetic field can shift the Co center from low- to high-spin (HS) state without atomic structure modification, affording one-order higher turnover frequency, a 50% increased H_2O_2 selectivity for ORR, and a ≈4000% magnetocurrent enhancement for OER. This catalyst can significantly minimize magnet usage, enabling safe and continuous production of a pure H_2O_2 solution for 100 h from a 100 cm^2 electrolyzer. The new strategy demonstrated here also applies to other metal phthalocyanine-based catalysts, offering a universal platform for studying spin-related electrochemical processes.

1. Introduction

The conversion and utilization of renewable energies often involve oxygen redox reactions (e.g., oxygen reduction reaction (ORR) and oxygen evolution reaction (OER)), which require efficient electrocatalysts to overcome their thermodynamic barriers and sluggish kinetics.[1] The recent development of single-atom catalysts by embedding individual transition metal atoms in nitrogen-doped carbon matrices (M-N-C) provides near-unity atomic utilization and good performance.[2] The binding strength of various oxygen redox reaction intermediates to the metal site through the hybridization of metal-3*d* and oxygen-2*p* orbitals have been proposed as performance governing factors.[3] Therefore, significant efforts have been devoted to optimize metal center electronic properties by tailoring catalyst atomic structures, such as the coordination number, coordinating atoms or ligands, and functional groups grafted near the metal atoms.[4]

As a fundamental electronic property, the active metal center spin state has been recently proposed as a catalytic performance descriptor for ORR and OER. The magnetic moment of the metal active center, one of the pristine electronic properties, has been identified as a performance descriptor to correlate electronic structures with electrochemical activity. A higher magnetic moment is usually associated with a high-spin (HS) state, which can facilitate the adsorption and activation of $*O_2$ (* stands for a surface adsorption site) toward *OOH formation and the spin-flip transition required for generating triplet O_2 from the doublet *OH intermediate, resulting in varied oxygen redox reaction performance.[5] E.g., by tuning the secondary coordination environment, the spin state of a manganese single atom active center could be shifted from LS to HS, affording improved H_2O_2 synthesis performance.[6] Other than alternating magnetic properties of an active center by changing its atomic structure, previous studies also showed that catalytic performance for oxygen redox reactions changes significantly under magnetic fields.[7] Except for Kelvin and Lorentz forces-induced mass transfer effects,[8] the magnetic field-induced spin state changes and spintronic effects have been assigned as the main contributors to activity enhancement on ferromagnetic metal, metal oxide, and metal

Z. Yu, Y. Wang, F. Liu, F. She, J. Chen, Y. Chen, L. Wei
School of Chemical and Biomolecular Engineering
The University of Sydney
Darlington, NSW 2006, Australia
E-mail: yuan.chen@sydney.edu.au; l.wei@sydney.edu.au
Z. Yu, D. Zhang, H. Li
Advanced Institute for Materials Research (WPI-AIMR)
Tohoku University
Sendai 980–8577, Japan
E-mail: li.hao.b8@tohoku.ac.jp
Y. Zhang, Z. Zeng
Department of Materials Science and Engineering
City University of Hong Kong
83 Tat Chee Avenue, Kowloon, Hong Kong 999077, China
R. Wang, L. Song
National Synchrotron Radiation Laboratory
Chinese Academy of Sciences Center for Excellence in Nanoscience
University of Science and Technology of China
Hefei, Anhui 230029, China
The ORCID identification number(s) for the author(s) of this article can be found under https://doi.org/10.1002/adma.202408461

DOI: 10.1002/adma.202408461

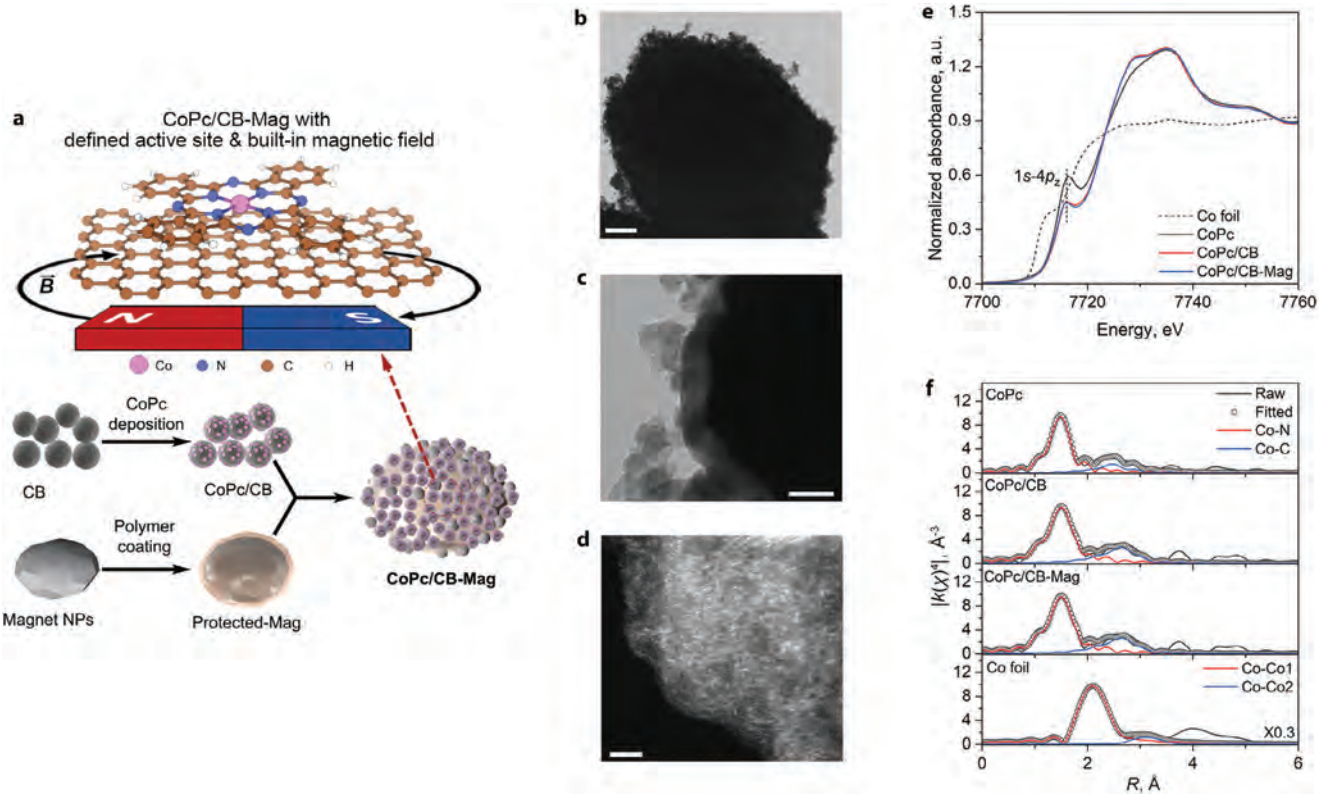

Figure 1. Catalyst synthesis and structural characterization. a) Scheme showing the synthesis of the CoPc/CB-Mag catalyst. b,c) BF-TEM images and d) a HAADF-STEM image of CoPc/CB-Mag. (Scale bar = 200, 100, and 2 nm in b, c, and d, respectively). e) Co K-edge XANES and f) Fitted EXAFS of CoPc/CB-Mag with reference samples.

sulfide catalysts.[9] It has also been applied to bimetallic cobalt-manganese and cobalt-iron metal-organic frameworks (CoMn- and CoFe-MOFs) using an alternating electromagnetic field.[10] The renormalization treatment could reconfigure the disordering low-spin to HS state, improve water dissociation kinetics, and optimize carrier transportation, resulting in significantly enhanced OER performance. However, these phenomena have been rarely reported for M-N-C catalysts.

Meanwhile, the spin manipulation also depends on how a magnetic field is applied. External magnetic fields ranging from a few hundred mT to a few T were typically applied by placing large permanent magnets near testing electrodes or spiring electromagnetic coils outside reactor vessels, which raise safety concerns and have limited process scalability.[9a,b,11] Therefore, due to the lack of M-N-C catalysts with well-defined active centers and the difficulties in manipulating their spin state without atomic structure modification, observing the spin-dependent oxygen redox reactions activity of M-N-C catalysts remains challenging.

Herein, we developed a new class of hierarchically structured heterogeneous molecular catalysts with an integrated magnetic field to address these challenges simultaneously. Metal(II) phthalocyanines (MPc), which bear a structure-defined M-N_4 active center with appreciable electrocatalytic activities and unique magnetic properties, were selected as the molecular precursor.[12] They were deposited on a conductive carbon black substrate (MPc/CB) and further anchored on polymer-protected permanent magnet nanoparticles, forming a hierarchically structured catalyst, denoted as MPc/CB-Mag, with defined and fully exposed M-N_4-C active sites and a built-in magnetic field for spin manipulation. Exemplified by cobalt phthalocyanines, the successful low-spin to HS transition of the Co(II) in CoPc/CB-Mag could substantially improve ORR and OER performance. Compared to CoPc/CB, it exhibits a 20% higher Faradaic efficiency for hydrogen peroxide (FE_{H2O2}) up to 90% and nearly one-order high site-specific turnover frequency (TOF) in the ORR test. It also shows a 143-mV reduced overpotential for reaching 10 mA cm^{-2} and improved OER kinetics. It can be easily employed in a 100 cm^2 two-electrode electrolyzer, realizing continuous and stable pure H_2O_2 production over 100 h with minimized magnet usage. Moreover, this strategy applies to other MPc/CB-Mag catalysts and magnetic metal oxide catalysts, where spin-dependent M-O interaction is critical.

2. Result and Discussion

2.1. Catalyst Preparation and Characterizations

Figure 1a illustrates the three-step catalyst synthesis approach. First, CoPc molecules were uniformly deposited on a carbon black (Vulcan XC-72R) substrate and are denoted as CoPc/CB (see details in the Experimental Section). The as-received CB substrate was purified to avoid interference from surface oxygenous groups (Figures S1 and S2, Supporting Information).[4c] The CoPc/CB catalyst shows a surface morphology comparable

to the pristine CB substrate under the observation of bright-field transmission electron microscopy (BF-TEM) without observable CoPc aggregates (Figure S3, Supporting Information). Its X-ray diffraction (XRD) pattern and specific surface area (309 m^2 g^{-1}, SSA) are also comparable to that of the pristine CB (Figures S4 and S5 and Table S1, Supporting Information). A Co mass loading of ≈0.28 wt.% was determined by inductively coupled plasma atomic emission spectroscopy (ICP-AES) test. Energy dispersive X-ray spectroscopy (EDX) elemental mapping performed under scanning TEM mode (STEM) further confirmed the uniform distribution of Co and N in CoPc/CB (Figure S6, Supporting Information).

Next, a catalytic inert and acidic electrolyte tolerant polydopamine (PDA) layer was coated on neodymium-iron-boron (NdFeB) magnet nanoparticles (≈500–1000 nm in diameter) by in situ polymerization. TEM characterization suggests the PDA layer has a thickness of ≈50–60 nm (Figure S7, Supporting Information) and constitutes ≈5 wt.% by thermal gravimetric analysis (TGA, Figure S8, Supporting Information). The PDA layer can protect the magnet well during a 4-day leaching test in a 0.1 M $HClO_4$ solution, a common acidic electrolyte for ORR (Figures S9–S11, Supporting Information).

The as-prepared CoPc/CB is mixed with PDA-protected magnets at a 1:3 mass ratio in isopropanol. This mass ratio is sufficient to form a monolayer coating of CoPc/CB on the PDA-protected magnets based on our estimation (using an average carbon black diameter of 30 nm and a magnet particle SSA of 13 m^2 g^{-1}, see detailed discussion and Figure S12, Supporting Information). The solvent was evaporated gradually, and the polymer layer worked as a "glue" to anchor CoPc/CB, affording the CoPc/CB-Mag catalyst. This catalyst offers well-defined and fully exposed Co-N_4 active catalytic sites inherent in CoPc molecules. Its hierarchical structure design allows a built-in magnetic field always near active sites, no matter whether deposited on a glassy carbon disk electrode (GCD) for intrinsic activity evaluation or assembled into a gas-diffusion electrode (GDE) for electrolyzer test. The introduction of insulating polymer-coated magnets would slightly increase the catalyst resistivity from 0.63 to 5.59 ohm cm^{-1} for CoPc/CB and CoPc/CB-mag catalysts. Nevertheless, the magnetic material usage in electrolyzers can be reduced significantly to a milligram level, up to seven orders smaller than earlier reports (see detailed comparison in Table S2, Supporting Information).[9b,11,13]

BF-TEM images (Figure 1b,c) of CoPc/CB-Mag show that CoPc/CB is successfully anchored on the smooth surface of the PDA-encapsulated magnetic particles. Sparsely distributed bright dots, i.e., single Co atoms in the dispersed CoPc molecules, can be found in the high-angle annular dark-field (HAADF, Figure 1d) STEM image focused on a single CB nanoparticle. We investigated the Co local atomic environment by Co K-edge X-ray absorption near-edge structure (XANES) and X-ray absorption fine structure (EXAFS). Figure 1e compares the XANES spectra of CoPc, CoPc/CB and CoPc/CB-Mag with that of Co foil. The prominent pre-edge peak at ≈7716 eV can be assigned to the $1s \rightarrow 4p_z$ transition of the Co-N_4 site with a D_{4h} symmetry in the CoPc molecules. Compared to CoPc, the reduced intensity of this pre-edge peak found in CoPc/CB and CoPc/CB-Mag is indicative of the slightly distorted Co-N_4 symmetry (e.g., to C_{4v}) due to the interaction between the CoPc molecule and the CB substrate. Our differential charge distribution calculation results showed that the adsorbed CoPc molecule would lose ≈0.317|e| to the carbon substrate (Figures S13 and S14, Supporting Information). This strong charge transfer phenomenon would be beneficial for the efficient electron transfer between CoPc and the carbon substrate. The EXAFS spectra of CoPc/CB and CoPc/CB-Mag displayed in Figure 1f are identical, suggesting that the local magnetic field has negligible impact on the Co center atomic structure. Fitting results also afforded identical Co coordination numbers (CN, close to 4, Table S3, Supporting Information). Compared to CoPc (1.946 Å), the carbon substrate surface curvature induced a slightly expanded Co-N bond length in CoPc/CB (1.963 Å) and CoPc/CB-Mag (1.966 Å). However, the EXAFS fitting, and the subsequent wavelet-transformed EXAFS analysis (Figure S15, Supporting Information) revealed negligible differences between CoPc/CB and CoPc/CB-Mag, suggesting the magnetic field had minimum impact on the atomic structure of the CoPc molecules.

2.2. Magnetic Property and Spin State Measurement

Background-corrected magnetic susceptibility versus temperature ($(\chi-\chi_0)$-T) plots suggests that bulk CoPc molecules and CoPc/CB are paramagnetic, and the purified CB substrate is diamagnetic (Figure S16, Supporting Information). Linear fitting of the $(\chi-\chi_0)^{-1}$ versus T plots (**Figure 2a**) afforded Curie constants (C) that lead to comparable effective magnetic moments (μ_{eff}, $\mu_{eff} = (8C)^{1/2}$) for pristine CoPc (2.487) and CoPc/CB (2.502). Electron paramagnetic resonance (EPR, Figure S17, Supporting Information) found comparable g factors for CoPc (2.849) and CoPc/CB (2.790). Their spin density (S), as determined by $\mu_{eff} = g(S(1+S))^{1/2}$, is 0.571 and 0.561 per Co atom, respectively. These values confirm that Co^{2+} in both samples are low spin (LS). Figure 2b compares the mass-normalized magnetic hysteresis loop of different samples. Pristine CoPc, CoPc/CB, and CB substrate all exhibit zero remanence. In contrast, the magnet core in CoPc/CB-Mag contributes a large saturation magnetization and coercivity of 125.9 emu g^{-1} and 6788 Oe, respectively, which can manipulate the Co spin state effectively. The diamagnetic CB substrate has negligible influence on the paramagnetic CoPc, allowing the built-in magnetic field to control the Co spin state in CoPc/CB-Mag.

X-ray spectroscopic methods were applied to assess the Co spin states in different samples. Figure 2c compares the high-resolution core-level Co 2p X-ray photoelectron spectra (XPS) of different samples. Due to the spin-orbital splitting, all samples exhibit two main peaks at ≈780 eV (Co $2p_{3/2}$) and ≈796 eV (Co $2p_{1/2}$). Unlike the spin transition found for CoPc molecules deposited on a Ag(111) surface, the spectra of CoPc and CoPc/CB are identical with a comparable splitting energy of 15.7 eV, suggesting the interaction between the CoPc and the carbon substrate has a negligible impact the cobalt electronic structure.[14] Satellite peaks due to the shake-up effects during electron ionization can be identified at ≈2 eV above the main Co $2p_{3/2}$ and $2p_{1/2}$ peaks.[14,15] The intensity ratio between the satellite and the main Co $2p_{3/2}$ peak ($I_{ratio} = I_{sat.}/(I_{sat.}+I_{main})$), which has been used to assign the spin state of cobalt complexes qualitatively, was found to be ≈0.22 and agrees with earlier reports.[16] These analysis

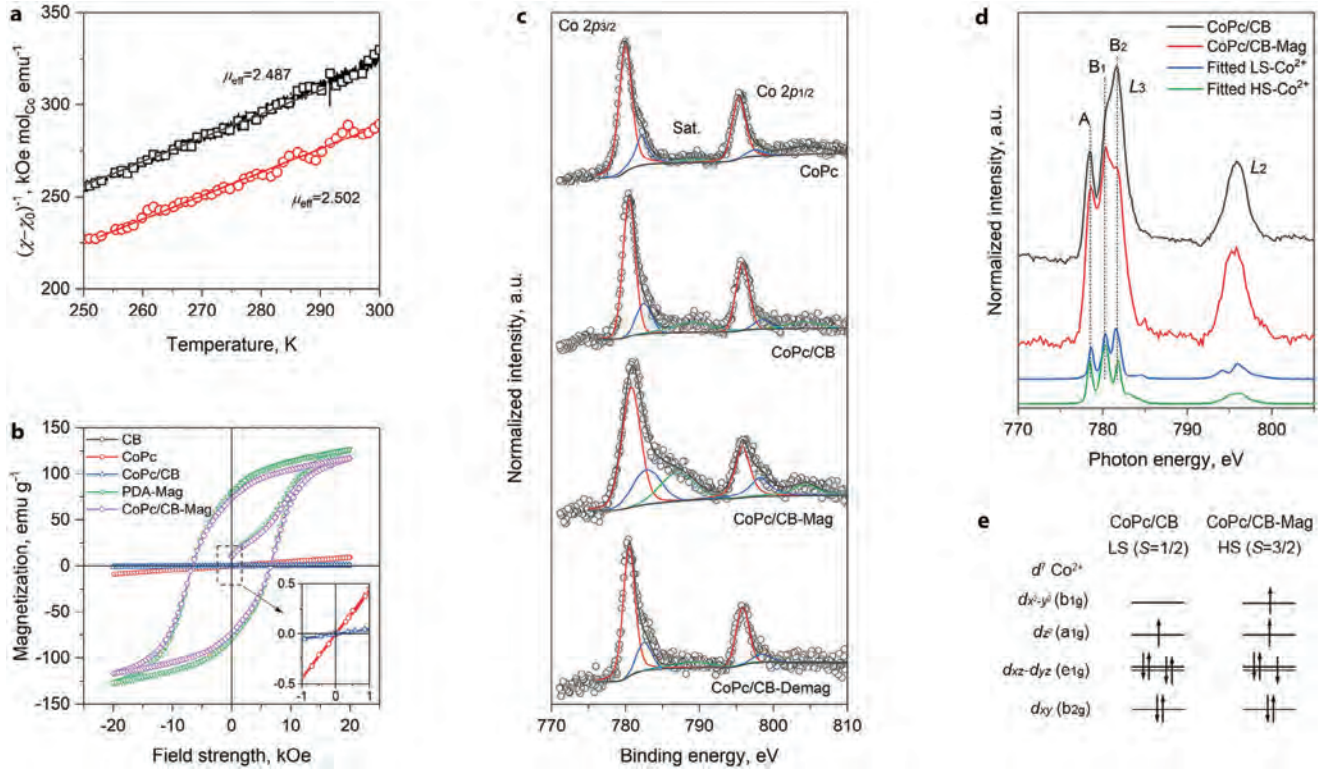

Figure 2. Magnetic property and electron spin state of CoPc/CB-Mag catalyst. a) Magnetic susceptibilities, and b) hysteresis loops of different samples. c) Co 2*p* XPS spectra of bulk CoPc, CoPc/CB, CoPc/CB-Mag, and CoPc/CB-Demag samples. d) Co L-edge XAS spectra of CoPc/CB and CoPc/CB-Mag catalysts. e) Scheme of Co spin states in CoPc/CB to CoPc/CB-Mag.

results collectively confirmed that the CoPc and CoPc/CB have an LS-Co^{2+} center. We further thermally demagnetized the Nd-FeB magnet in Ar flow at 400 °C for 30 min. This temperature is well above the magnet Curie temperature (310–370 °C) but not too high to deteriorate the magnet crystal structure (Figure S18, Supporting Information). Polymer coating was applied, and an additional sample was prepared following the same method. This sample was denoted as CoPc/CB-Demag, and its XPS spectrum is identical to that of the CoPc and CoPc/CB, suggesting that the polymer coating has no impact on the Co electronic properties.

With the magnetic field, the splitting energy of the CoPc/CB-Mag catalyst has slightly decreased by 0.1 eV. The intensive satellite peak that emerged at ≈787.3 eV can be attributed to the interaction of the 2*p* core hole with additional unpaired electrons in the 3*d* level. The peak intensity ratio ($I_{ratio} = I_{sat.}/(I_{sat.}+I_{main})$) has also increased significantly to 0.44, confirming the spin transition to an HS-Co^{2+}.[16] Moreover, the spectroscopic changes in the Co $2p_{1/2}$ region are examined from the spectra difference between different samples. As shown in Figure S19 (Supporting Information), the CoPc/CB-Mag catalyst exhibits obvious increments in the Co $2p_{1/2}$ region (795–805 eV) in comparison to CoPc, CoPc/CB, and CoPc/CB-Demag, while CoPc/CB and CoPc/CB-Demag are indifferent. Collectively, we can conclude that the LS-Co in the paramagnetic CoPc could be transformed to HS under the external magnetic field.

The Co spin state transition was further confirmed by Co L-edge XAS features, which are originated from the transition of 2*p* electron to unoccupied 3*d* orbitals. As shown in Figure 2d, similar to Co 2*p* XPS, CoPc/CB, and CoPc/CB-Mag, all exhibit L3 and L2 peaks separated by ≈15 eV due to the spin-orbit coupling. Three major peaks at 778.4 (A), 780.2 (B_1), and 781.6 (B_2) eV can be identified in the L_3 edge, corresponding to electron transitions into empty orbitals which are perpendicular (A) or parallel (B_1 and B_2) to the *x*-*y* plane.[17] We find that the line shape of CoPc/CB agrees with earlier reports and the fitted spectrum using the CTM4XAS6.1, corresponding to an LS Co^{2+} in the ground state of $b_{2g}{}^2e_g{}^4a_{1g}{}^1$.[18] Under the built-in magnetic field, these peaks exhibit negligible position shifts but apparent intensity changes. The increased intensity of Peak A can be attributed to the creation of a half-filled d_{xz}-d_{yz} orbital in HS-Co^{2+}, as shown in Figure 2e, providing additional empty components in the direction perpendicular to the *x*-*y* plane. Meanwhile, the relative intensity changes between Peaks B_1 and B_2 reflect the occupation change in the d_{xz}-d_{yz} (e_{1g}) and the d_{x2-y2} (b_{1g}) orbitals. The transition from LS to HS-Co creates an additional half-filled d_{xz}-d_{yz} orbital, resulting in the intensified Peak B_1. Meanwhile, the reduced peak intensity of B_2 is caused by the filling of the d_{x2-y2} orbital. Meanwhile, the energy separation between peak A and the intensity-weighted center of peak B_1 and B_2 has reduced from 2.7 to 1.6 eV, suggesting a reduced crystal field splitting energy (CFSE) in CoPc/CB-Mag.[19] The simulated spectrum of HS Co^{2+} in D_{4h} symmetry using this CFSE value also agrees well with the experimental results. The characterization results confirm the spin state under an external field. The significant increment in the HS population can be attributed to the synergy between the

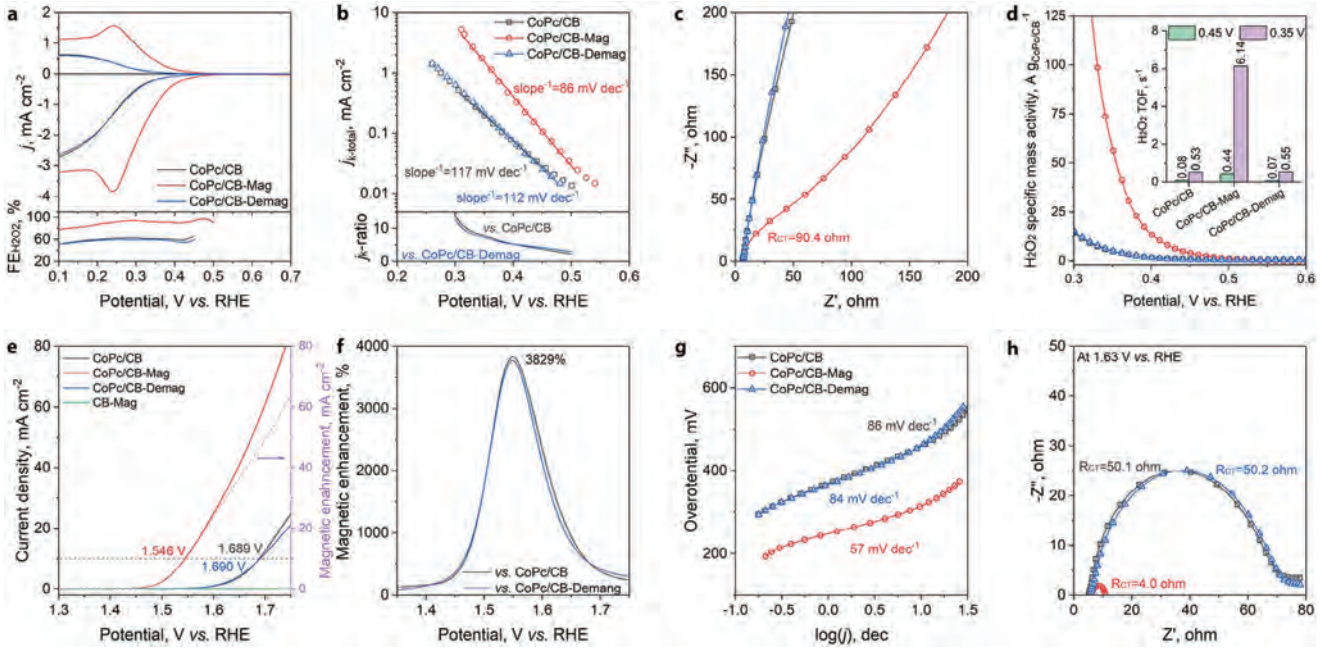

Figure 3. Electrochemical performance. a–d) ORR performance. a) LSV curves (top panel) and corresponding FE_{H2O2} (bottom panel), b) kinetic current densities ($j_{K\text{-}H2O2}$, top panel) and the j_k ratios of CoPc/CB-Mag against others (bottom panel), c) EIS Nyquist plots and d) mass specific activity. The inset in (d) shows the site-specific TOF values at 0.35 and 0.45 V. e–h) OER performance. e) LSV curves, f) calculated magnetocurrent enhancement, g) Tafel plots, and h) EIS Nyquist plots.

altered energy splitting (Zeeman interaction) and spin-orbit coupling of the electrons in the CoPc molecule.[9c,20]

2.3. Electrochemical Performance Assessment

The ORR performance was first evaluated on a rotary ring-disk electrode (RRDE, with calibrated collection efficiency (N) = 0.249, Figure S20, Supporting Information) in an O_2-saturated 0.1 M $HClO_4$ electrolyte. The mass loading of different catalysts was kept at 0.025 mg cm^{-2} on a CoPc/CB basis. The CB substrate and polymer-protected magnetic nanoparticles showed negligible ORR activity (Figure S21, Supporting Information). As shown in **Figure 3a**, without the built-in magnetic field, CoPc/CB bearing an LS Co center shows moderate ORR activity comparable to previous reports.[21] It requires a potential of 0.43 and 0.39 V (vs a reversible hydrogen electrode, RHE) to reach an appreciable current density on the disk (–0.05 mA cm^{-2}) and ring (0.025 mA cm^{-2}) electrodes. The H_2O_2 Faradic efficiency (FE_{H2O2}) is ≈50–60% between 0.5 to 0.1 V (bottom panel of Figure 3a), corresponding to an H_2O_2 molar selectivity (X_{H2O2}) up to 74%.

The built-in magnetic field in CoPc/CB-Mag can significantly enhance activity, improving the disk and ring onset potentials by 60 and 90 mV to 0.49 and 0.48 V, respectively. A 30% increment of the current density (j) at 0.1 and 81 mV shift of the half-wave potential ($E_{1/2}$, taking the j at 0.1 V as the limit) are obtained. The FE_{H2O2} also increases to a maximum of ≈93%, corresponding to a X_{H2O2} >96%. The Figure 3b top panel further compares the total ORR kinetic current density ($j_{k\text{-}total}$) calculated by Koutecký-Levich equation (details in Experimental Section). The $j_{k\text{-}total}$ of CoPc/CB-Mag is up to an order higher than that of CoPc/CB or CoPc/CB-Demag (bottom panel of Figure 3b). Tafel analysis assigned an electron-coupled proton transfer step as a universal rate-limiting step, in good agreement with previously reported Co-based single-atom catalysts for acidic ORR.[22] Nevertheless, CoPc/CB-Mag has faster electron transfer kinetics with a reduced Tafel slope of 86 mV dec^{-1} compared to CoPc/CB (117 mV dec^{-1}) and CoPc/CB-Demag (112 mV dec^{-1}). From the electrochemical impedance Nyquist plots (EIS, Figure 3c), its charge-transfer resistance (R_{ct}, 91.4 ohm at 0.49 V) is also much smaller. The H_2O_2-specific activity is further compared by using the H_2O_2-specific kinetic current density ($j_{K\text{-}H2O2}$). The CoPc/CB-Mag can deliver an H_2O_2-specific mass activity of ≈56.3 A g_{cat}^{-1} and a site-specific turnover frequency (TOF) of 6.1 s^{-1} at 0.35 V (Figure 3d), which are over an order higher than CoPc/CB of 5.1 A g_{cat}^{-1} and 0.53 s^{-1}, respectively. Notably, all improved catalytic performances observed on CoPc/CB-Mag disappear on CoPc/CB-Demag, implying the critical role played by the built-in magnetic field.

Considering that the adsorption of various OER intermediates (e.g., OH*, OOH* and O_2*) on a single atom site all involve M-O interactions,[23] we further demonstrate that the built-in magnetic field could also impact these crucial steps and improve the OER activity of CoPc/CB-Mag. We prepared the catalyst by replacing the PDA polymer protecting layer with polyvinyl chloride (PVC), which has a better tolerance to alkaline electrolytes (Figure S22, Supporting Information). The OER LSV curves collected in a 1 M KOH electrolyte were compared in Figure 3e. Control experiments suggest that without CoPc, carbon black loaded with PVC-protected magnet shows negligible activity. The CoPc/CB-Mag catalyst exhibits an OER onset potential (defined as potential required to reach 0.5 mA cm^{-2}) of ≈1.46 V versus RHE, which is ≈164 mV lower CoPc/CB and

CoPc/CB-Demag. The overpotential required to reach 10 mA cm^{-2} (η_{10}), a common activity descriptor, has also decreased by 143 mV to 313 mV. The magnetocurrent, defined as the performance difference between the CoPc/CB-Mag and CoPc/CB catalysts, dominates the performance improvement, affording a maximum enhancement of 3829% at ≈1.56 V (Figure 3f). As expected, improved kinetic performance is confirmed by a smaller Tafel slope of 57 mV dec^{-1} (Figure 3g) and drastically reduced R_{ct}, i.e., from 50 ohms to 4 ohms with the built-in magnetic field (Figure 3h). The CoPc/CB-Mag also showed good stability. It can operate at 50 mA cm^{-2} continuously for 48 h with merely 34 mV potential increment (Figure S23, Supporting Information), which is superior to CoPc/CB. Moreover, we normalized the ORR and OER currents of different samples to their electrochemical surface area (ECSA), and the trend still stands (Figures S24–S27, Supporting Information), ruling out that the performance improvement was due to any catalyst morphology change after incorporation of the magnet nanoparticles. The built-in magnetic field can effectively boost the oxygen redox reaction activity of the Co-N_4 active center without atomic structure modification. It pushes its performance among the top of recently reported single-atom catalysts as compared to Tables S4 and S5 (Supporting Information).

2.4. The Role of the Built-in Magnetic Field

We attempt to understand the mechanism behind the improved electrochemical performance of the built-in magnetic field. The possible contribution of magnetic field-induced Lorentz and/or Kelvin effects was first considered.[7,8] The Lorentz force may create magnetohydrodynamic effects at the electrode surface, which allows efficient gas bubble removals and benefits gas-generating reactions (e.g., hydrogen and OERs).[8b] However, it cannot explain the improved ORR and OER onset potentials. The Lorentz force contribution can be further ruled out by the indifferent performance observed on diamagnetic IrO_2 or Co_3O_4 catalysts with or without the building magnetic field (Figure S28, Supporting Information). Previous studies also attributed the improved ORR performance of a commercial Pt/C catalyst to the Kelvin force-enhanced transportation of paramagnetic triplet O_2 under an external magnetic field.[13a] However, a Pt/C-Mag catalyst prepared by anchoring commercial Pt/C catalyst (20 wt.% Pt on Vulcan XC-72R) on the PDA-protected magnet nanoparticles showed no performance enhancement (Figure S29, Supporting Information). Considering the Kelvin force would only become significant when the field strength is sufficient to generate a large gradient (i.e., $\nabla \boldsymbol{B}$) along the reactant concentration gradient,[8a] the magnet nanoparticles used in the test will likely be too weak to impact the bulk diffusion of dissolved O_2. We placed a large magnet (≈320 mT) within 3–5 mm to the Pt/C catalyst. Again, no performance enhancement was found, ruling out the Kelvin force effects (Figures S30–S33, Supporting Information). In contrast, this magnet block can boost the performance of the CoPc/CB catalyst, although less effective, and requires a seven-order more magnet usage to our built-in magnetic fields (Figures S34 and S35, Supporting Information).

The Multiphysics simulation displayed in **Figures** 4a and S36 (Supporting Information) suggests that the magnetic flux originating from a 100 nm polymer layer-protected magnet nanoparticle (1000 nm diameter) would decay quickly in space, losing half of the flux within ≈200 nm from the surface, which is similar to large magnet blocks (Figures S37 and S38, Supporting Information) but on a much smaller spatial scale.[11a,13b] To further probe the relationship between the electronic properties and electrochemical activity of the Co center to the strength of the built-in magnetic field, we deposited a thick CoPc/CB layer (0.15 mg cm^{-2}, thickness ≈2.5 µm, Figure S39, Supporting Information) on top of a magnet nanoparticle layer (0.075 mg cm^{-2}, the same loading in ORR performance tests). The Co 2*p* XPS depth profile was then collected under Ar^+ plasma and displayed in Figure 4b. The intensity of the Co $2p_{3/2}$ satellite peak region (785–790 eV) increased gradually after the first ten etching repetitions and became saturated after 28–30 repetitions. This spatial dependence can be further quantitatively envisaged by the intensity ratio calculated between the satellite peak and the $2p_{3/2}$ peak ($I_{sat.}/I_{2p3/2}$, Figure 4c). Compared to the indifferent profile of a CoPc/CB layer (Figure S40, Supporting Information), the change of the profiles further confirms that the Co spin state manipulation is dependent on field strength.

Based on the XPS profiling and an estimated carbon etching rate of 1.25 nm s^{-1} (Experimental Section),[24] the influence of the magnetic layer becomes significant when the mass ratio between CoPc/CB and magnets is ≈1.25:1 and saturates at ≈0.38:1. Therefore, the mass ratio in our CoPc/CB-Mag (0.33:1) is sufficient to shift all the Co center from low-spin to HS. Additional CoPc/CB catalysts of different CoPc/CB-to-magnet mass ratios (X, X = 2, 1, 0.33, and 0.2) were prepared to simulate CoPc/CB under different field strengths. By keeping the CoPc/CB mass loading the same on the electrode (0.025 mg cm^{-2} for ORR and 0.1 mg cm^{-2} for OER), the experimental performance trend (Figure 4d,e) is in good agreement to the XPS measurement. The activity improves gradually with the X reducing from 2 to 0.33 and becomes stable at 0.2. Similar FE_{H2O2} and OER magnetocurrent enhancement are found for X = 0.33 and 0.2.

We then performed spin-polarized density functional theory (DFT) calculations on geometry-optimized models (Figure S14, Supporting Information). With the built-in magnetic field, the Co spin transition from LS to HS can increase the Co electronic spin moment (μ) from 0.153 μ_B to 0.653 μ_B, which is beneficial for oxygen redox reactions.[5d,25] As shown in Figure 4f, the partial density of state (pDOS) of Co *d*-electron shifted significantly. The HS Co *d*-band center up shifted by 73 meV to the Fermi level (E_F), enabling stronger binding with various oxygenous intermediates. The Co *d*-electron orbital energy levels were also differentiated (Table S6, Supporting Information) and displayed in Figure 4g. Considering the edge-on mode of the O_2 adsorption on the single-atom Co center, the M-O bond is formed by the hybridization of the O_2 π^* and the Co d_z^2 and d_{xz}-d_{yz} orbitals, and its hybridization level will determine the $^*O_2$ activation.[26] Compared to LS Co^{2+}, the 40 meV upshifted d_z^2 orbital in the HS Co^{2+} can offer stronger hybridization with the O_2 π^* orbital. Meanwhile, the down-shifted d_{xz}-d_{yz} orbitals will provide a less back donation to the O_2* antibonding π^* orbital, suppressing O-O bond activation and stabilizing OOH* toward H_2O_2 formation.[27] This analysis agrees with the stronger *OOH binding on the HS-Co site (1.96 eV) to that on the LS-Co site (3.42 eV), which could result in

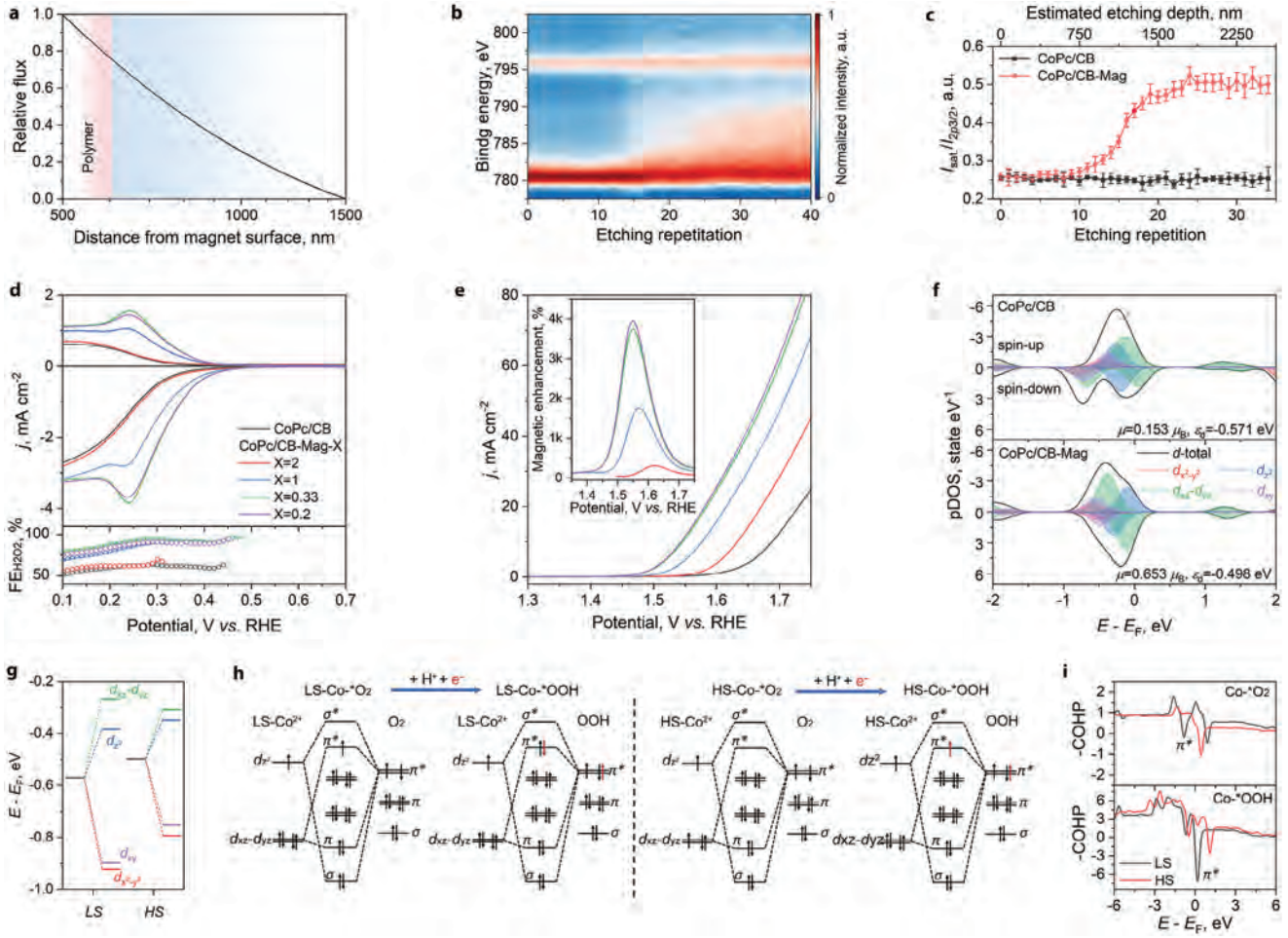

Figure 4. Understanding the role of the built-in magnetic field. a) Simulated relative magnetic flux of a 1 μm diameter magnet particle with a 100 nm thick polymer shell along the radius direction. b) Co 2*p* XPS depth profile, and c) the correlation between the Co $2p_{3/2}$ peak intensity ratio and the catalyst etching time/thickness. d) ORR and e) OER performance at different CoPc/CB to magnet mass ratios. Inset in (e) shows the OER magnetocurrent enhancement. Calculated f) Co *d*-electron pDOS and g) band energy structures of the LS- and HS-Co active sites. h) Proposed orbital interactions between Co sites with ORR intermediates and i) COHP analysis results.

a higher reaction rate for the *OOH formation. This observation agrees with the earlier reports where the *OOH binding strength is key in achieving highly selective H_2O_2 synthesis.[28] This theoretical analysis was further verified by thiocyanate (SCN^-) poisoning and H_2O_2 reduction reaction tests performed on the catalysts. The upshifted d_z^2 orbital of HS-Co site in CoPc/CB-Mag could also exhibit stronger binding to SCN^-, resulting in a greater $E_{1/2}$ change (98 mV vs 51 mV, Figure S41, Supporting Information) in the poisoning test. Meanwhile, the suppressed O-O bond activation of the HS-Co site also leads to a much inferior H_2O_2 reduction activity. CoPc/CB-Mag has 160 mV higher onset potential and ≈80% smaller H_2O_2 reduction current density at 0.2 V compared to LS-Co in the CoPc/CB (Figure S42, Supporting Information).

We further attempt to understand the improved kinetics of the CoPc/CB-Mag catalyst by illustrating the schematic molecular orbital hybridization diagrams in Figure 4h. Compared to LS-Co, O_2* or OOH* adsorbed HS-Co has an empty or half-filled π* orbital, which can result in higher bond orders to stabilize the adsorption of intermediates and improve ORR performance.[29] This assignment was further confirmed by the crystal orbital Hamilton population (COHP, Figure 4i) derived from the Co-O pDOS of *O_2 and *OOH adsorbed models (Figure S43, Supporting Information). The COHP analysis revealed the presence of antibonding (π*) orbitals near the Fermi level in the LS-Co-*O_2, which are absent in HS-Co-*O_2. Meanwhile, there are approximately two electrons in the π* orbital of LS-Co-*OOH, while only one electron is found for HS-Co-*OOH, near the Fermi level. It supports our initial hypothesis that, compared to LS-Co, the HS-Co site could afford an empty or half-filled π* orbital with *O_2 and *OOH, resulting in stronger binding of these adsorbates. It is noteworthy that the unpaired electron in the Co d_{x2-y2} orbital of the HS-Co is unaffected since it will not participate in the Co-O bonding process in the atop oxygen adsorption model.

Moreover, the incorporation of a free electron in the OOH* formation step (O_2* + H^+ + e^- → OOH*) is favored on HS-Co site. Since, its empty π* orbital can accept an electron with either

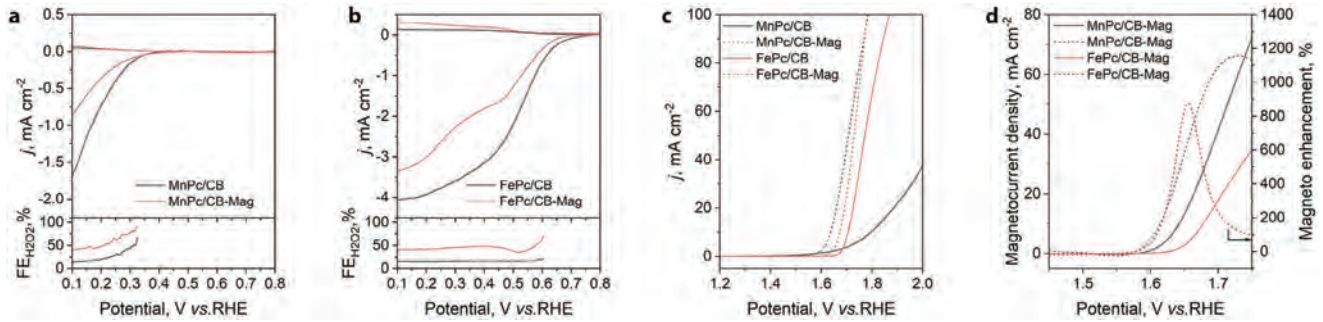

Figure 5. Expanding to other MPc-based catalysts. a,b) ORR performance collected in a 0.1 M $HClO_4$ electrolyte. a) MnPc/CB and MnPc/CB-Mag, and b) FePc/CB and FePc/CB-Mag catalysts. c,d) OER performance tested in a 1 M KOH electrolyte. c) OER LSV curves. d) Calculated OER magnetocurrent and the relative enhancement.

a spin-up or spin-down state by considering the electron spin angular momentum conservation.[5b,e] This non-spin selection accelerates the electron transfer kinetics, which agrees with experimentally observed Tafel slopes discussed earlier (Figure 2c,g). Similarly, during the OER process, this spin-flip transition could overcome the transformation barrier of the doublet *OH to the triplet O_2.[30] After all, the magnetic field-induced spin polarization could effectively align the electron spin and facilitate favorable spin transition, enhancing OER kinetics.

2.5. Extending to Other MPc/CB-Mag and Metal Oxide Catalysts

Finally, we demonstrate that our strategy can serve as a universal platform to study the spin-dependent electrochemical activity of other MPc-based catalysts, e.g., MnPc and FePc-based HMCs. The corresponding MPc/CB and MPc/CB-Mag catalysts were prepared and characterized (Figures S44–S46 and Table S7, Supporting Information). They exhibit identical morphology to that of the CoPc/CB and are paramagnetic with an effective spin moment of 3.81 and 1.87 μ_B for Mn and Fe, respectively. The different L-edge XAS spectra can be attributed to the spin-state manipulation by the built-in magnetic field.

Their ORR and OER performance were collected following the same testing methods. The ORR LSV curves and the calculated FE_{H2O2} are compiled in **Figure 5**a,b, showing varied activity changes under the influence of the built-in magnetic field. MnPc/CB-Mag and FePc/CB-Mag exhibited reduced disk currents and improved FE_{H2O2}, i.e., from less than 20% to over 50% at 0.1 V. Their OER LSV curves are compared in Figure 5c. With the built-in magnetic field, the overpotential required for delivering 10 mA cm^{-2} has reduced by 160 ± 2 and 33 ± 1 mV for Mn and Fe, respectively. The MnPc/CB-Mag catalyst shows the greatest enhancement up to 1200% as shown in Figure 5d. Tafel analysis and EIS measurement results also confirm improved kinetic performance (Figures S47 and S48, Supporting Information). In addition, this built-in magnetic field strategy is also applicable to some metal oxide OER catalysts, e.g., NiO, $NiZnFeO_4$, and $CoMnVO_4$ (Figures S49–S51 and Table S8, Supporting Information), offering a promising universal approach to enhance the performance of alkaline water electrolysis.

2.6. Safe and Efficient H_2O_2 Production from a Two-Electrode Electrolyzer

Usually, a large magnet block is required to provide magnetic fields with sufficient strength for influencing electrochemical reactions. The mass ratio between magnet and catalysts is usually over 10^4 (Table S2, Supporting Information), bringing potential safety risks and challenges in device/process scaling-up.[9b,11] At a mass ratio of only 3, up to seven orders smaller to recent reports, the amounts of magnetic materials required in this CoPc/CB-Mag can be significantly reduced to improve process safety and scalability. We can easily apply the CoPc/CB-Mag catalyst on a 100 cm^2 electrode (**Figure 6**a) to assemble an electrolyzer (Figures S52 and S53, Supporting Information) with improved H_2O_2 production performance. Protons are provided from IrO_2-catalyzed anodic OER across a Nafion 212 proton exchange membrane and a 1 mm thick solid-state porous electrolyte assembled by a cation exchange resin (Figure S54, Supporting Information) to the cathode. Electrolytic ion-free H_2O_2 solutions are produced with a deionized water flowing phase.[31]

The potential-current response curves (Figure 6b) of the electrolyzer using CoPc/CB-Mag and CoPc/CB catalysts were collected without internal resistance (*i*R) correction. By eliminating the O_2 diffusion limits, CoPc/CB-Mag can deliver a current density of up to 300 mA cm^{-2} at a full cell voltage of 4.27 V, which is ≈44% smaller than that of the CoPc/CB (6.16 V). We further operated the cell at 100 mA cm^{-2} for 50 h continuously, and the cell voltage responses are compared in Figure 6c. With the built-in magnetic field, the CoPc/CB-Mag electrode can stably produce an electrolytic ion-free H_2O_2 solution at ≈2.99 V with a small cell voltage increment of ≈75 mV after 50 h. It also exhibits a stable FE_{H2O2} of ≈90% during the test. At a water flow rate of 30 mL h^{-1}, the H_2O_2 concentration in the effluent can reach 16.0 wt.% (by $Ce(SO_4)_2$ titration, Figure S55, Supporting Information), which corresponds to an H_2O_2 productivity of 1.68 mmol cm^{-2} h^{-1} or 16.79 mol g_{cat}^{-1} h^{-1} (CoPc/CB basis). By further increasing the operation current to 200 mA cm^{-2}, it can further reach an H_2O_2 productivity of 3.10 mmol cm^{-2} h^{-1}. On the contrary, CoPc/CB shows much inferior performance. It requires ≈4.14 V to reach 100 mA cm^{-2} and exhibits a greater voltage increment (233 mV) after the test. It also delivers a much lower FE_{H2O2}, ≈42%, which is only half that of CoPc/CB-Mag. We further recovered the post-electrolysis catalyst from the electrode by sonication and

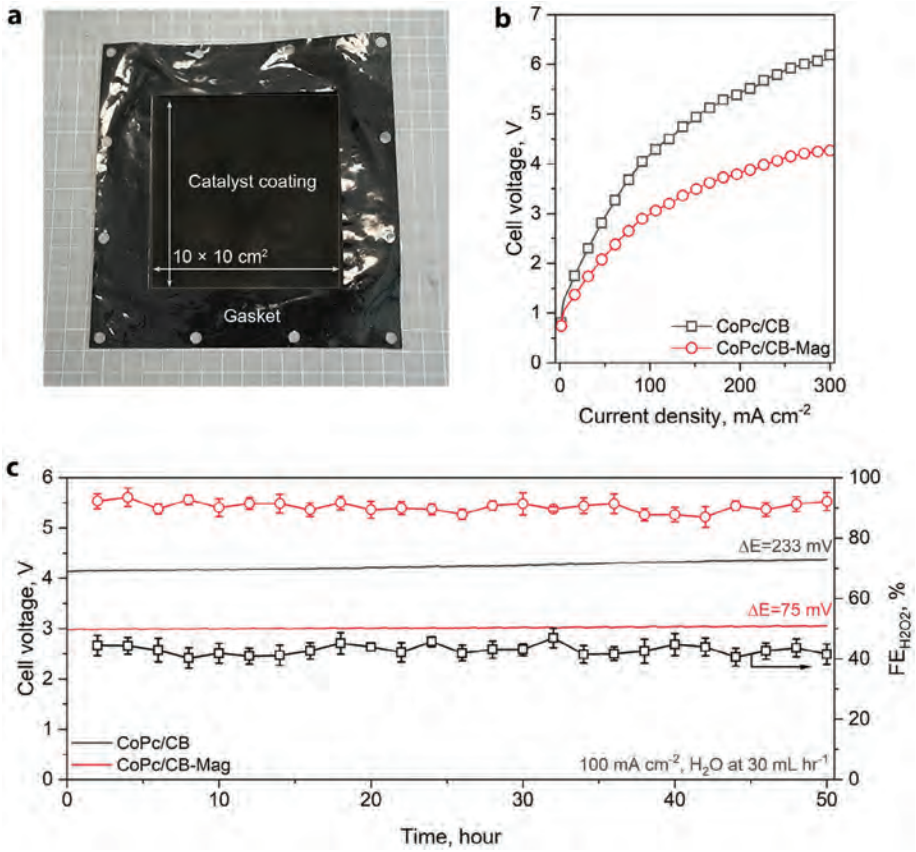

Figure 6. Application of the CoPc/CB-Mag catalyst in a two-electrode electrolyzer. a) A photo of a 100 cm^2 electrode. b) Current-potential responses, and c) continuous H_2O_2 production performance of different catalysts at 100 mA cm^{-2} and a DI water flow rate of 30 mL h^{-1}. All cell voltages are reported without iR-correction.

characterized the catalyst properties (Figure S56, Supporting Information). Its Co L-edge spectrum still resembled an HS-Co center, identical to the fresh catalyst. The polymer coating and CoPc/CB particles are also observable under TEM characterization. The Raman spectra of the pristine and tested catalysts.

3. Conclusion

In summary, we demonstrated a new class of heterogeneous molecular catalysts with a built-in magnetic field. The spin state of well-defined paramagnetic single-atom catalytic active sites can be manipulated without altering their atomic structure. As showcased by the CoPc, control experiments exclude the possible efforts from magnetic Lorentz and Kelvin forces, attributing the catalytic performance improvement solely to the built-in magnetic field, which promotes an LS to HS transition of the Co active center. Molecular orbital interaction analysis and DFT calculation results suggest that the HS-Co site could stabilize the *OOH intermediate and facilitate the formation of H_2O_2 in ORR. The magnetic field could also effectively align the electron spins to facilitate favorable spin transition during OER, overcoming the kinetic barrier to transition the doublet *OH to the triplet O_2. The electrocatalyst can be readily applied in two-electrode electrolyzers with orders that lower the need for magnets, resulting in improved electrolyzer energy efficiency and H_2O_2 productivity. Importantly, only small amounts of magnetic nanomaterials would be required to create such hierarchically structured heterogeneous molecular catalysts, which improves process safety and scalability in studying spin state transitions and enabling more efficient electrochemical processes. Moreover, this strategy also demonstrated tunable catalytic activities of other transition metal phthalocyanine-based catalysts, as exemplified by Mn and Fe, or ferromagnetic metal oxide catalysts, providing a universal platform for studying the spin-dependent activity of such single-atom catalysts.

4. Experimental Section

Materials: Metal phthalocyanine molecules (MPc, *β*-form, MnPc, 99%; CoPc, 99%; FePc, 90%; NiPc, 85%), cerium(IV) sulfate ($Ce(SO_4)_2$, 99.99%), *N,N*-dimethylformamide (DMF, ≥99%), isopropanol (IPA, 99.9%), Nafion 117 solution (5%), nitric acid (HNO_3, 70%), perchloric acid ($HClO_4$, 70%,), dopamine hydrochloride, tris(hydroxymethyl) aminomethane hydrochloride (Trizma, >99%), polyvinyl chloride (PVC, low molecular weight, M_w ≈48000), cyclohexanone (≥99.0%), triphenylphosphine (Ph_3P, 99%), potassium hydroxide (KOH, semiconductor grade), and Nafion 212 membrane (thickness 0.002′) were obtained from Sigma-Aldrich. CB (Vulcan XC-72R) and the core/shell Ir/IrO_x catalyst were purchased from Fuelcell Store. Argon (Ar, 99.999%) and oxygen (O_2, 99.999%) gas cylinders were obtained from BOC Gas Australia. NdFeB (≈800–1000 nm in size) permanent magnet nanoparticles were

purchased from Nanochemazone. Deionized water (18 MΩ cm^{-1}) was produced from a lab water purification system (Milli-Q). MPc molecules were purified by triple sublimation before being used for catalyst synthesis. Other chemicals were used as received.

Preparation of Polymer Shell-Encapsulated Magnetic Nanoparticles: A polydopamine (PDA) shell was coated to avoid possible corrosion of the magnet particles. Briefly, 50 mg of the as-received magnet powder was dispersed in a 50 mL tris buffer (10 mM, pH = 7). Afterward, another 10 mL of tris buffer (10 mM) containing 100 mg dopamine hydrochloride was added under vigorous stirring (2500 rpm), and the solution pH was adjusted to 8.5 to initiate dopamine polymerization to form a PDA coating on mag powder. The mixture was further mechanically stirred for 12 h at room temperature, and the PDA-coated mag (PDA-mag) was recovered by filtration, followed by ethanol washing and drying in an oven overnight. We also prepared PDA-coated demagnetized nanoparticles following the same method, except the particles were thermally annealed under Ar at 400 °C (well above its Curie temperature at ≈310–370 °C). The PDA-coated demagnetized nanoparticles were also recharged for reference experiments.

A PVC polymeric shell was coated on magnetic nanoparticles to avoid their potential corrosion during electrochemical reactions in alkaline electrolytes. ≈100 mg of PVC powder was first dissolved in 4 mL of cyclohexanone under stirring at 70 °C to form a homogeneous solution. Afterward, 500 mg of NdFeB magnetic powder was added to the solution under sonication. The solution was further stirred, the solvent was slowly removed by heating, and the viscous mixture was added dropwise to ethanol under vigorous stirring. The particulate solids were then recovered by centrifugation and washed with ethanol before they were finally dried under vacuum at 60 °C overnight.

Synthesis of HMCs: Prior to catalyst preparation, the CB substrate was purified by annealing in a 5% H_2/Ar gas flow at 1500 °C for 2 h to clean the surface. The CoPc/CB catalyst was synthesized by depositing CoPc on CB. ≈5 mg of CoPc and 50 mg of CB were dissolved in 50 mL DMF. After 30 min ultrasonication, the mixture solution was further stirred under Ar protection for 24 h before the solids were recovered by filtration. The solids were washed with DMF and ethanol before being dried in a vacuum oven at 80 °C overnight. Afterward, as-prepared CoPc/CB was mixed with PDA-coated magnetic particles at a mass ratio of 0.33:1 in IPA. After bath sonication for 30 min, the mixture was first gradually dried by evaporation and then dried in a vacuum oven at 80 °C overnight. The resulting catalyst was denoted as CoPc/CB-Mag. Other catalysts of different mass ratios were also prepared. Using the same method, CoPc/CB-Demag was also synthesized using the polymer-coated demagnetized nanoparticles. Other MPcs (M = Mn, Fe, and Ni) were used to prepare MPc/CB and MPc/CB-Mag catalysts following the same method.

Characterizations: Catalyst resistivity was measured on a powder resistivity tester (ST2722, Suzhou Jingge Electronics Inc.) with 1 MPa applied pressure to compact the powder sample. Scanning electron microscope images were collected on a Zeiss Ultraplus microscope. Spherical aberration-corrected HAADF-STEM images were obtained on an FEI Themis-Z microscope. TEM images of the magnetic particles were obtained on a JEOL JEM-2200 microscope operating at 100 kV. The metal loading of catalysts was determined by ICP-AES on a Perkin Elmer Avio 500 spectrometer. Magnetic properties of different materials were collected on a DynaCool (Quantum Design) physical property measurement system. Temperature-dependent magnetic susceptibility was measured from 2 to 300 K at 10000 Oe. Saturation hysteresis was measured at 2 K and 300 K between −20000 to 20000 Oe. Curie constant (C) was obtained by linear fitting of the inverse of magnetic moment against temperature, and the effective magnetic moment (μ_{eff}) and the spin density S were calculated using the equations below:

$$\mu_{eff} = \sqrt{8C} = g\sqrt{S^2 + S)} \quad (1)$$

where g was determined from EPR spectra recorded on a Bruker EMXnano spectrometer in operating with X-band at room temperature. To activate small amounts of Co single atom sites, overdosed Ph_3P was added according to a reported method.[32] The g-factor was calculated using:

$$g = 71.4484 \cdot \nu/B \quad (2)$$

where ν is the testing frequency in GHz and B is the field strength in mT.

XPS spectra were collected on a Thermo Scientific K-Alpha+ spectrometer using an Al-Kα source (1486.3 eV). Samples were loaded on an Au substrate. The Co L-edge XAS spectra were collected on beamlines MCD-A and MCD-B at Soochow Beamline for Energy Materials, National Synchrotron Radiation Laboratory (NSRL) of China. The fitting of the Co L-edge spectra was performed using CTM4XAS6.1 software for the Co^{2+} in D_{4h} symmetry, with the initial state set as $2p^6$-$3d^7$ and the final state as $2p^5$-$3d^8$. The values of the crystal field parameters, including 10Dq, Dt and Ds, were obtained from experimental spectra and the DFT calculated orbital energies.

XPS Etching Rate Estimation: The Co 2p depth profile of the CoPc/CB layer deposited on the magnet layer was collected by Ar^+ (2 keV) etching with a primary ion current density of 0.1 mA cm^{-2}. The spectra were collected every 60 s initially until the observable Co spectra line shape was noticed, and the collection interval was reduced to 20 s. The etching rate, V, was estimated using the following equation:[24]

$$V = \frac{MSj_P}{\rho N_A e} \quad (3)$$

where M and ρ are the molar mass and density of the target, which is 12 × 10^{-3} kg mol^{-1} and 2000 kg m^{-3} for CB, respectively. N_A is the Avogadro number (6.02 × 10^{23} mol^{-1}), and e is the electron charge (1.6 × 10^{-19} C). S is the sputtering yield (0.2 atoms per ion), and j_P is the primary ion current density (0.1 mA cm^{-2}). An etching rate of ≈1.25 nm s^{-1} was obtained by using Equation (3), leading to a total etched catalyst of 1350 nm. A CoPc/CB layer without the underlying magnet layer was also prepared, and Co XPS profiles were obtained under a similar condition.

Electrochemical Tests: Electrochemical performance tests were carried out using a conventional three-electrode configuration on an Autolab PGSTAT302N electrochemical workstation at 25 °C. An RRDE (E6R1, Pine Research, with a calibrated collection efficiency of 0.249) equipped with a GCD and a Pt ring was used for testing ORR performance in a 0.1 M $HClO_4$ (pH = 1.3) electrolyte. A glassy carbon tip RDE (E3PK, Pine Research) was used for OER in a 1 M KOH electrolyte (pH = 13.6). An Ag/AgCl electrode (3 M KCl filling, Basi, MF-2056) and a graphite rod electrode (AFCTR3B, Pine Research) were used as the reference and counter electrodes, respectively, for ORR. A Hg/HgO with 1 M KOH filling is used as reference electrode for OER. All reported potentials were calibrated against RHE. The catalyst ink was prepared by dispersing 5 mg of as-synthesized catalysts in 1 mL water/ethanol solution (1/9 = v/v, containing 0.05% Nafion 117) by 30 min bath sonication. For ORR test, the CoPc/CB-Mag mass loading was kept at 0.1 mg cm^{-2}, otherwise stated. CoPc/CB was deposited at 0.025 mg cm^{-2} to keep the same Co mass loading. For OER test, the mass loading was increased to 0.4 mg cm^{-2} for CoPc/CB-Mag and 0.1 mg cm^{-2} for CoPc/CB. LSV polarization curves were recorded at 5 mV s^{-1} without iR-compensation for all tests. The magnetocurrent is calculated as the OER current density difference between the MPc/CB and MPc/CB-Mag catalysts.

As for ORR, the Pt ring electrode was biased at 1.2 V versus RHE to collect the ring current (i_{ring}). The H_2O_2 selectivity (H_2O_2%) and Faradaic efficiency (FE) were calculated using the following equation:

$$FE = \frac{i_{ring}}{N} / |i_{disk}| \times 100\% \quad (4)$$

$$H_2O_2\% = 200 \times \frac{\frac{i_{ring}}{N}}{|i_{disk}| + \frac{i_{ring}}{N}} \quad (5)$$

The kinetic limiting current density j_K was extracted from the polarization curves using the Koutecký-Levich (K-L) equations shown below:

$$\frac{1}{j_{disk}} = \frac{1}{j_L} + \frac{1}{j_K} = \frac{1}{B\omega^{1/2}} + \frac{1}{j_K} \quad (6)$$

where j_{disk}, j_L and j_K are the disk diffusion limiting and kinetic current densities, respectively, ω, is the angular velocity. Tafel analysis was performed by using the extracted j_K. The H_2O_2-specific current density ($j_{K\text{-}H2O2}$) and the turnover frequency (TOF, s^{-1}) of the catalysts were calculated by Equations (7) and (8):

$$j_{K-H2O2} = j_K \times FE\% \quad (7)$$

$$TOF = j_{K-H2O2} / (0.025 \times \text{Co wt}\%/Mw_{Co}) / (2 \times F) \quad (8)$$

where 0.025 is the CoPc/CB mass loading, Co wt.% is the Co mass loading in the catalyst as determined by ICP-AES, F is the Faraday constant (96485 C mol^{-1}), and Mw_{Co} is the molar weight of Co (59 g mol^{-1}). Similarly, the OER TOF was calculated by Equation (9):

$$TOF = j_{K-H2O2} / (0.1 \times \text{Co wt}\%/Mw_{Co}) / (4 \times F) \quad (9)$$

where 0.1 is the mass loading of CoPc/CB in mg cm^{-2}.

Thiocyanate Poisoning and H_2O_2 Reduction Reaction Test: The LSV curve was collected in an O_2-saturated 0.1 M $HClO_4$ electrolyte with or without the addition of 50 mM KSCN. The CoPc/CB mass loading was kept at 0.025 mg cm^{-2}. The scan rate was 5 mV s^{-1}. The H_2O_2 reduction activity was assessed in an Ar-saturated 0.1 M $HClO_4$ electrolyte with 100 mM H_2O_2 at a scan rate was 5 mV s^{-1}.

Flow-Cell Electrolyzer Test: CoPc/CB-Mag and CoPc/CB catalysts were deposited on a carbon paper gas diffusion electrode (10 × 10 cm^2, Toray TGP-H-090 with 30% Teflon) at 0.2 mg cm^{-2} on CoPc/CB basis by spray coating. IrO_2/Ir nanoparticles were deposited on a Ti felt at 1 mg cm^{-2} and hot pressed on a Nafion 212 membrane as the anode for OER. A 0.5 M H_2SO_4 anolyte was circulated at 10 mL h^{-1}. Humified O_2 gas was injected in the cathode chamber at a flow rate of 200 sccm. A poly(divinylbenzene) copolymer cationic exchange resin (CGC50 × 8, batch#015X/10/0, ≈30–50 µm, Purolite) was used as a porous solid-state electrolyte. Deionized water flow was supplied by a peristaltic pump to wash out the as-produced H_2O_2 at ≈6 mL min^{-1}, and the effluent was collected for analysis. The electrochemical performance of the electrolyzer was collected on a Gamry Reference 3000 workstation coupled with a Reference 30K Booster.

H_2O_2 Concentration Determination: The H_2O_2 concentration (C_{H2O2}) in the solution produced by the electrolyzer was determined by a $Ce^{+3/+4}$ titration method. The UV–vis absorbance at 316 nm was used to establish the calibration curve. The yellow Ce^{4+} solution can be converted to colorless Ce^{3+} following the reaction: $2Ce^{4+} + H_2O_2 \rightarrow 2Ce^{3+} + 2H^+ + O_2$. Then C_{H2O2} can be calculated from:

$$C_{H_2O_2} = \frac{1}{2} \cdot \Delta C_{Ce^{4+}} \quad (10)$$

Computational Methods: Spin-polarized DFT calculations were carried out using the Vienna ab initio simulation package (VASP) program.[33] The ion-electron interaction was described by the projector-augmented wave (PAW) method while the electron exchange correlation was described by the Perdew-Burke-Ernzerhof (PBE) functional within the generalized gradient approximation (GGA). Spin polarization can check the possibility of a magnetic ground state, which be calculated by setting the command of MAGMOM. The final magnetic moment of Co atom in the LS state (MAGMOM = 0) and high spin state (MAGMOM = 1) is 0.15 and 0.69 μ_B, respectively. A cutoff energy of 400 eV was applied for the plane-wave basis set. The energy and force convergence thresholds were set to 10^{-5} eV and 0.05 eV $Å^{-1}$, respectively. The vacuum space was set to 16 Å to avoid the interaction between the supercell and its periodic images along the *z*-direction.

Supporting Information

Supporting Information is available from the Wiley Online Library or from the author.

Acknowledgements

Z.Y. and D.Z. contributed equally to this work. This work is financially supported by the Australian Research Council under the Future Fellowship (FT210100218) and Discovery Project (DP230101694), JSPS KAKENHI (JP23K13703), and The University of Sydney under the External Research Collaboration Seed Funding (G221867). The authors acknowledge the National Computational Infrastructure (NCI, NCMAS-2024-59), Center for Computational Materials Science, Institute for Materials Research, Tohoku University for the use of MASAMUNE-IMR (202312-SCKXX-0203 and 202312-SCKXX-0207) and the Institute for Solid State Physics (ISSP) at the University of Tokyo for the computational resources. The authors are grateful for the beam time at Soochow Beamline for Energy Materials at NSRL and the resin gifted from Purolite Pty Ltd.

Open access publishing facilitated by The University of Sydney, as part of the Wiley - The University of Sydney agreement via the Council of Australian University Librarians.

Conflict of Interest

A provisional patent application (AU2024901482) has been submitted.

Data Availability Statement

The data that support the findings of this study are available from the corresponding author upon reasonable request.

Keywords

heterogeneous molecular catalysts, magnetic enhancement, oxygen evolution reaction (OER), oxygen reduction reaction (ORR), spintronics

Received: June 14, 2024
Revised: August 29, 2024
Published online: September 17, 2024

[1] a) J. Masa, C. Andronescu, W. Schuhmann, *Angew. Chem., Int. Ed.* **2020**, *59*, 15298; b) H. Yang, X. Han, A. I. Douka, L. Huang, L. Gong, C. Xia, H. S. Park, B. Y. Xia, *Adv. Funct. Mater.* **2021**, *31*, 2007602.

[2] a) Q. Shi, S. Hwang, H. Yang, F. Ismail, D. Su, D. Higgins, G. Wu, *Mater. Today* **2020**, *37*, 93; b) C. Zhu, S. Fu, Q. Shi, D. Du, Y. Lin, *Angew. Chem., Int. Ed.* **2017**, *56*, 13944; c) H. Fei, J. Dong, D. Chen, T. Hu, X. Duan, I. Shakir, Y. Huang, X. Duan, *Chem. Soc. Rev.* **2019**, *48*, 5207.

[3] a) Z. W. Seh, J. Kibsgaard, C. F. Dickens, I. Chorkendorff, J. K. Nørskov, T. F. Jaramillo, *Science* **2017**, *355*, eaad4998; b) K. Maiti, S. Maiti, M. T. Curnan, H. J. Kim, J. W. Han, *Adv. Energy Mater.* **2021**, *11*, 2101670; c) Y. Wang, D. Wang, Y. Li, *Adv. Mater.* **2021**, *33*, 2008151.

[4] a) C. Tang, L. Chen, H. Li, L. Li, Y. Jiao, Y. Zheng, H. Xu, K. Davey, S.-Z. Qiao, *J. Am. Chem. Soc.* **2021**, *143*, 7819; b) E. Jung, H. Shin, B.-H. Lee, V. Efremov, S. Lee, H. S. Lee, J. Kim, W. Hooch Antink, S. Park, K.-S. Lee, S.-P. Cho, J. S. Yoo, Y.-E. Sung, T. Hyeon, *Nat. Mater.* **2020**, *19*, 436; c) B. H. Lee, H. Shin, A. S. Rasouli, H. Choubisa, P. F. Ou, R. Dorakhan, I. Grigioni, G. H. Lee, E. Shirzadi, R. K. Miao, J. Wicks, S. Park, H. S. Lee, J. Q. Zhang, Y. J. Chen, Z. Chen, D. Sinton, T. Hyeon, Y. E. Sung, E. H. Sargent, *Nat. Catal.* **2023**, *6*, 234.

[5] a) C. Fontanesi, *Curr. Opin. Electrochem.* **2018**, *7*, 36; b) S. Bhattacharjee, S.-C. Lee, *J. Phys. Chem. C* **2018**, *122*, 894; c) Z. Zhang, P. Ma, L. Luo, X. Ding, S. Zhou, J. Zeng, *Angew. Chem., Inter. Ed.* **2023**, *62*, 202216837; d) W. Zhong, Y. Qiu, H. Shen, X. Wang, J. Yuan, C. Jia, S. Bi, J. Jiang, *J. Am. Chem. Soc.* **2021**, *143*, 4405; e) J. Gracia, M. Fianchini, C. Biz, V. Polo, R. Gómez, *Curr. Opin. Electrochem.* **2021**, *30*, 100798; f) Y. Sun, S. Sun, H. Yang, S. Xi, J. Gracia, Z. J. Xu, *Adv. Mater.* **2020**, *32*, 2003297; g) L. Hu, F. Wang, Y. Jing, *J. Phys. Chem. Lett.* **2023**, *14*, 11429; h) X. Wei, C. Jiang, H. Xu, Y. Ouyang, Z. Wang, C. Lu, X. Lu, J. Pang, F. Dai, X. Bu, *ACS Catal.* **2023**, *13*, 15663.

[6] L.-Y. Dong, J.-S. Wang, T.-Y. Li, T. Wu, X. Hu, Y.-T. Wu, M.-Y. Zhu, G.-P. Hao, A.-H. Lu, *Angew. Chem., Int. Ed.* **2024**, *63*, 202317660.

[7] S. Luo, K. Elouarzaki, Z. J. Xu, *Angew. Chem., Int. Ed.* **2022**, *61*, 202203564.

[8] a) L. M. A. Monzon, J. M. D. Coey, *Electrochem. Commun.* **2014**, *42*, 42; b) L. M. A. Monzon, J. M. D. Coey, *Electrochem. Commun.* **2014**, *42*, 38.

[9] a) T. Sun, Z. Tang, W. Zang, Z. Li, J. Li, Z. Li, L. Cao, J. S. Dominic Rodriguez, C. O. M. Mariano, H. Xu, P. Lyu, X. Hai, H. Lin, X. Sheng, J. Shi, Y. Zheng, Y.-R. Lu, Q. He, J. Chen, K. S. Novoselov, C.-H. Chuang, S. Xi, X. Luo, J. Lu, *Nat. Nanotechnol.* **2023**, *18*, 763; b) F. A. Garcés-Pineda, M. Blasco-Ahicart, D. Nieto-Castro, N. López, J. R. Galán-Mascarós, *Nat. Energy* **2019**, *4*, 519; c) J. Yan, Y. Wang, Y. Zhang, S. Xia, J. Yu, B. Ding, *Adv. Mater.* **2021**, *33*, 2007525.

[10] a) G. Zhou, P. Wang, H. Li, B. Hu, Y. Sun, R. Huang, L. Liu, *Nat. Commun.* **2021**, *12*, 4827; b) P. Huang, M. Meng, G. Zhou, P. Wang, W. Wei, H. Li, R. Huang, F. Liu, L. Liu, *Proc. Natl. Acad. Sci. USA* **2023**, *120*, 2219661120.

[11] a) C. Hunt, Z. Zhang, K. Ocean, R. P. Jansonius, M. Abbas, D. J. Dvorak, A. Kurimoto, E. W. Lees, S. Ghosh, A. Turkiewicz, F. A. Garcés Pineda, D. K. Fork, C. P. Berlinguette, *J. Am. Chem. Soc.* **2022**, *144*, 733; b) S. S. Bhargava, D. Azmoodeh, X. Y. Chen, E. R. Cofell, A. M. Esposito, S. Verma, A. A. Gewirth, P. J. A. Kenis, *ACS Energy Lett.* **2021**, *6*, 2427.

[12] J. Bartolomé, C. Monton, I. K. Schuller, in *Molecular Magnets: Physics and Applications*, Springer, Heidelberg **2014**, pp. 221–245.

[13] a) N. I. Wakayama, T. Okada, J.-i. Okano, T. Ozawa, *Jpn. J. Appl. Phys.* **2001**, *40*, L269; b) T. Okada, N. I. Wakayama, L. Wang, H. Shingu, J.-i. Okano, T. Ozawa, *Electrochim. Acta* **2003**, *48*, 531.

[14] M. Schmid, A. Kaftan, H.-P. Steinrück, J. M. Gottfried, *Surf. Sci.* **2012**, *606*, 945.

[15] a) D. C. Frost, C. A. McDowell, I. S. Woolsey, *Chem. Phys. Lett.* **1972**, *17*, 320; b) D. Briggs, V. A. Gibson, *Chem. Phys. Lett.* **1974**, *25*, 493.

[16] Y. G. Borod'ko, S. I. Vetchinkin, S. L. Zimont, I. N. Ivleva, Y. M. Shul'ga, *Chem. Phys. Lett.* **1976**, *42*, 264.

[17] a) J. Uihlein, H. Peisert, M. Glaser, M. Polek, H. Adler, F. Petraki, R. Ovsyannikov, M. Bauer, T. Chassé, *J. Chem. Phys.* **2013**, *138*, 081101; b) E. Annese, J. Fujii, I. Vobornik, G. Panaccione, G. Rossi, *Phys. Rev. B* **2011**, *84*, 174443.

[18] a) J. Bartolomé, C. Monton, I. K. Schuller, in *Molecular Magnets*, Springer, Berlin/New York **2014**, pp. 221–245; b) E. Stavitski, F. M. F. de Groot, *Micron* **2010**, *41*, 687.

[19] D. K. Bora, X. Cheng, M. Kapilashrami, P. A. Glans, Y. Luo, J.-H. Guo, *J. Synchrotron Rad.* **2015**, *22*, 1450.

[20] D. Dai, H. Xiang, M.-H. Whangbo, *J. Comput. Chem.* **2008**, *29*, 2187.

[21] A. Morozan, S. Campidelli, A. Filoramo, B. Jousselme, S. Palacin, *Carbon* **2011**, *49*, 4839.

[22] T. Shinagawa, A. T. Garcia-Esparza, K. Takanabe, *Sci. Rep.* **2015**, *5*, 13801.

[23] a) Y. Dong, C. W. Oloman, E. L. Gyenge, J. Su, L. Chen, *Nanoscale* **2020**, *12*, 9924; b) Z. Zhou, Z. Pei, L. Wei, S. Zhao, X. Jian, Y. Chen, *Energy Environ. Sci.* **2020**, *13*, 3185.

[24] K. Wasa, in *Handbook of Sputtering Technology*, 2nd Edition, (Eds: K. Wasa, I. Kanno, H. Kotera), William Andrew Publishing, Oxford **2012**, pp. 41–75.

[25] Y. Sun, J. Wang, Q. Liu, M. Xia, Y. Tang, F. Gao, Y. Hou, J. Tse, Y. Zhao, *J. Mater. Chem. A* **2019**, *7*, 27175.

[26] A. Kulkarni, S. Siahrostami, A. Patel, J. K. Nørskov, *Chem. Rev.* **2018**, *118*, 2302.

[27] K. Liu, J. Fu, Y. Lin, T. Luo, G. Ni, H. Li, Z. Lin, M. Liu, *Nat. Commun.* **2022**, *13*, 2075.

[28] a) S. Xu, Y. Yu, X. Zhang, D. Xue, Y. Wei, H. Xia, F. Zhang, J.-N. Zhang, *Angew. Chem., Int. Ed.* **2024**, *63*, 202407578; b) J. Gao, H. b. Yang, X. Huang, S.-F. Hung, W. Cai, C. Jia, S. Miao, H. M. Chen, X. Yang, Y. Huang, T. Zhang, B. Liu, *Chem* **2020**, *6*, 658.

[29] Y. Sun, X. Ren, S. Sun, Z. Liu, S. Xi, Z. J. Xu, *Angew. Chem., Int. Ed.* **2021**, *60*, 14536.

[30] a) L. Li, J. Zhou, X. Wang, J. Gracia, M. Valvidares, J. Ke, M. Fang, C. Shen, J.-M. Chen, Y.-C. Chang, C.-W. Pao, S.-Y. Hsu, J.-F. Lee, A. Ruotolo, Y. Chin, Z. Hu, X. Huang, Q. Shao, *Adv. Mater.* **2023**, *35*, 2302966; b) S. Xu, S. Feng, Y. Yu, D. Xue, M. Liu, C. Wang, K. Zhao, B. Xu, J.-N. Zhang, *Nat. Commun.* **2024**, *15*, 1720.

[31] C. Xia, Y. Xia, P. Zhu, L. Fan, H. Wang, *Science* **2019**, *366*, 226.

[32] a) X. Li, A.-E. Surkus, J. Rabeah, M. Anwar, S. Dastigir, H. Junge, A. Brückner, M. Beller, *Angew. Chem., Int. Ed.* **2020**, *59*, 15849; b) M. Baumgarten, C. J. Winscom, W. Lubitz, *Appl. Magn. Reson.* **2001**, *20*, 35.

[33] G. Kresse, J. Furthmüller, *Phy. Rev. B* **1996**, *54*, 11169.